Check for updates

P4VP–Ru[II](bda) polyelectrolyte–metal complex as water oxidation catalyst: on the unique slow-diffusion and multi-charge effects of the polyelectrolyte ligand†

Tao Zheng,‡[a] Mo Zhu,‡[a] Muhammad Waqas,[a] Ahmad Umair,[a] Muhammad Zaheer,[a] Jinxian Yang,[a] Xiaozheng Duan [ID] *[b] and Lianwei Li [ID] *[a]

In this work, we analyze the catalytic mechanism of P4VP–Ru[II](bda) polyelectrolyte–metal complex (PMC) as a water oxidation catalyst and elucidate how the unique slow diffusion and multi-charge properties of the polyelectrolyte ligand dominate the catalytic process. Four poly(4-vinyl pyridine)–Ru(bda) (P4VP–Ru) PMCs with different chain lengths and controlled Ru loading amounts were prepared and used as catalysts for catalytic water oxidation. These catalysts present excellent catalytic performance with turnover numbers (TON) from ∼1200 to ∼1700 because of the good hydration properties. Surprisingly, the combined catalysis kinetics and kinetic isotope effect (KIE) studies for P4VP–Ru PMCs confirm the single-site water nucleophilic attack (WNA) mechanism in catalysis, rather than the interaction between two metal oxide units (I2M). A combination of dynamic light scattering characterization, zeta-potential measurement and molecular dynamics simulation reveals that the slow diffusion and multi-charge properties of the polyelectrolyte ligand are responsible for the observed mechanism difference between the P4VP–Ru PMC system and small-molecule multi-nuclear system, though the two systems actually own a similar structural feature (flexible linkages between Ru centers). Our experimental and simulation results highlight the fact that though the existence of flexible linkages between Ru centers could provide large conformation entropy for the occurrence of Ru-dimerization in small-molecule and neutral polymer systems, the entropy elasticity could not overcome the electrostatic interaction energy in the PMC system. Clearly, this work unambiguously clarified why both intra-chain and inter-chain Ru-dimerization (I2M) are prohibited for the PMC system from a perspective of macromolecular chemistry and physics.

Introduction

As one of the most classic types of cationic polyelectrolytes, the quaternized/protonated poly(4-vinyl pyridine) (P4VP) has found broad applications in drug delivery,[1,2] antibacterial materials,[3,4] corrosion inhibition,[5,6] solar cells,[7,8] *etc.* Among various applications, the development of novel polymer–metal complexes as efficient catalysts for catalytic organic synthesis and energy conversion is one of the hottest topics in the past decade.[9]

[a]*Department of Chemical Physics, University of Science and Technology of China, Hefei, Anhui 230026, China. E-mail: llw@mail.ustc.edu.cn*

[b]*State Key Laboratory of Polymer Physics and Chemistry, Changchun Institute of Applied Chemistry, Chinese Academy of Sciences, Changchun, Jilin 130022, China. E-mail: xzduan@ciac.ac.cn*

† Electronic supplementary information (ESI) available: Details of the ^{1}H-NMR spectra of all samples, the original schematic diagrams and data of some calculation results, the UV-vis spectra of one P4VP–Ru, the experimental setups of GC and oxygen sensor measurement and the $f(R_h)$ of P4VP–Ru complexes and their corresponding P4VP precursors. See DOI: 10.1039/c8ra08012g
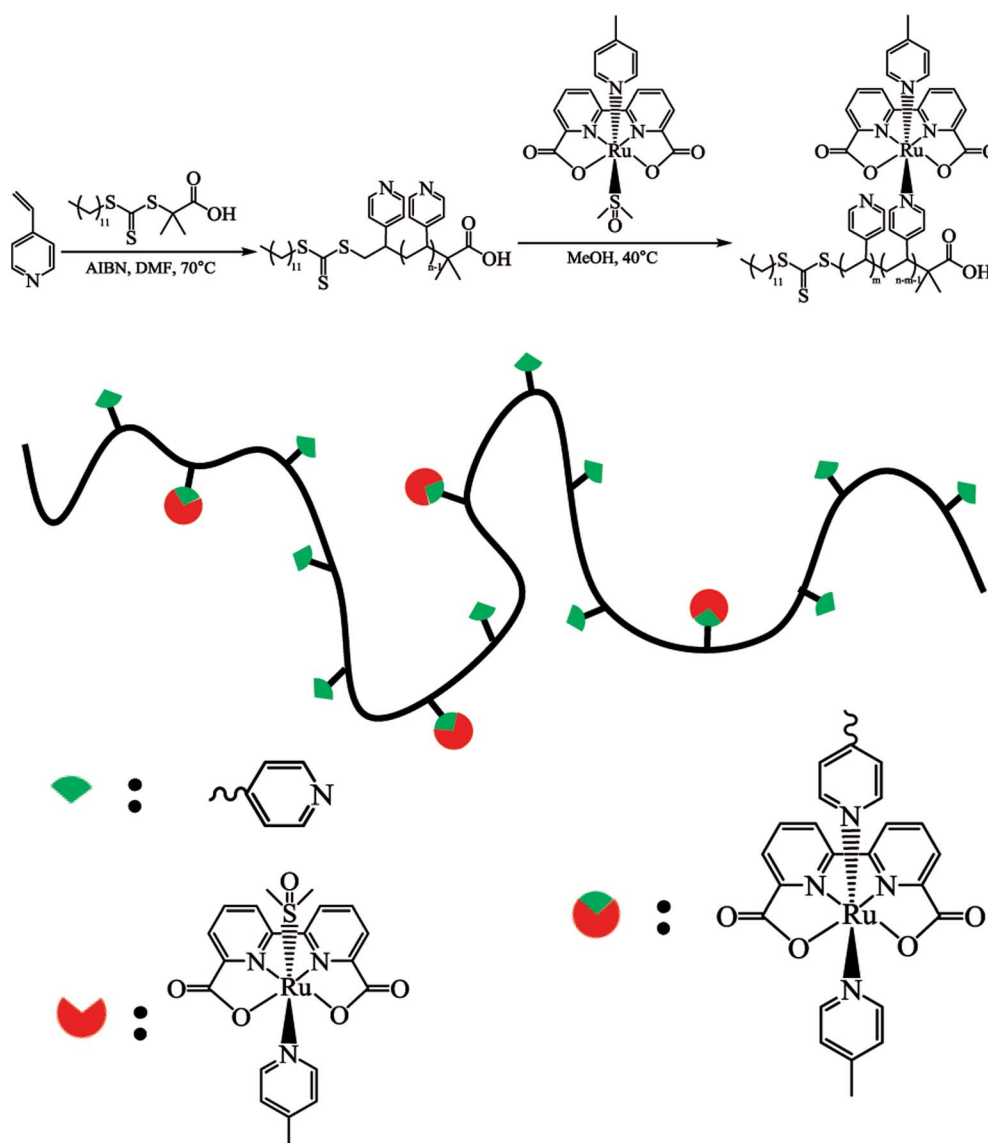
‡ Tao Zheng and Mo Zhu contributed equally to this work.

Due to the strong electron-donating ability of the pyridine ring, P4VP shows great potential in coordination with various transition metal ions to form polymer–metal complexes. To date, a number of examples of P4VP–metal complexes have been reported to show high activities for catalyzing organic reactions.[10–14] However, in most of the previous reports, the used P4VP–metal complexes were normally cross-linked and heterogeneous in nature, *i.e.*, they were neither soluble nor ionized in water. Generally, the heterogeneous catalytic system could provide a convenience for easier separation and recycling of catalysts from the reaction system, but simultaneously sacrifices the opportunity for the deep understanding of the structure–property correlation at a molecular level. For heterogeneous catalysis, the thermal motion of polymer segments is greatly prohibited due to the "frozen" state of chain segments, which ultimately results in the prohibition of possible cooperative catalytic effect originating from neighboring centers. In addition, if the catalysis product is poorly soluble in the reaction medium, the heterogeneous catalyst might be encapsulated in the product and eventually lose its catalytic activity.

Such a situation has indeed been previously reported in the study of hydrogenation of 4-nitrophenol catalyzed by a heterogeneous catalyst.[15] It is worth pointing out that the P4VPs were typically used as polymer ligands in previous related studies,[10–14] whereas how the chain length dependent properties affect the catalysis process has never been explored experimentally.

So far, the interaction between the polymer ligand and metal center remains unclear in most of previous studies, and how the polymer ligand effect influences the catalytic performance as well as the catalytic mechanism has been scarcely investigated. By a careful comparison of small-molecule ligands and polymer ligands, it is obvious that the greatest difference lies in the chain length-dependent properties, such as the unique slow-diffusion and multi-charge properties of polymer ligand.[16] However, how these polymer effects influence the catalytic performance and mechanism for a given polymer–metal catalytic system has never been seriously considered.

In this work, we illustrate how to utilize the unique slow diffusion and multi-charge properties of polyelectrolyte ligand to regulate the catalytic performance and mechanism. Specifically, we report the preparation and catalysis study of four P4VP–Ru^{II}(bda) polyelectrolyte–metal complexes (PMCs) with different chain lengths as polymer catalysts for homogeneous water oxidation (Scheme 1), where bda is 2,2′-bipyridine-6,6′-dicarboxylate. The P4VP–Ru catalyst was designed based on the following rationales: (1) [Ru(bda)(L)$_2$] (L: donor ligand) is one of the most widely studied water oxidation catalysts (WOCs) showing high activities;[17–19] (2) the chain length of P4VP can be tailored *via* controlled polymerization to regulate the polymer coil size as well as the diffusion coefficient of P4VP–Ru complex in aqueous solution; (3) P4VP–Ru with different loading amounts of Ru can be easily prepared by the efficient ligand exchange reaction between pyridine unit of P4VP and precursor [Ru(bda)(pic)(DMSO)] (pic = 4-picoline); (4) the acidic aqueous

Scheme 1 Schematic synthesis of P4VP–Ru polymer–metal complex by a combination of RAFT polymerization and pyridine/DMSO exchange reaction.

solution (pH = 1.0) is typically used for Ru(bda) based catalytic studies, which endows protonated P4VP ligand with multi-charge property.

The above advantages facilitate the present study on the influence of slow diffusion and multi-charge effects of PMC catalysts on the catalytic mechanism and performance in water oxidation reaction. Our previous studies of polymer-based catalysts for heterogeneous water reduction and oxidation reactions lay the foundation of present work.[20–22] This work has revealed, for the first time, that the slow diffusion and multi-charge effects of macromolecular ligand play important roles in determining the catalytic mechanism and performance for the PMC-catalyzed water oxidation reaction.

Results and discussion

The reversible addition-fragmentation chain transfer (RAFT) polymerization was utilized for the synthesis of four poly(4-vinyl pyridine) (P4VP) samples with controlled molar mass distributions but different chain lengths (Scheme 1). The final products were obtained after 48 h of polymerization at 70 °C. A combination of H-nuclear magnetic resonance (^{1}H-NMR), size exclusion chromatography (SEC) and Fourier transform infrared spectroscopy (FTIR) measurements confirms the structural information of prepared samples. First, the ^{1}H-NMR spectra (Fig. S1 and S2†) show both the signals of protons from RAFT agent (protons a–d) and polymer backbone (protons e–i) for P4VPs. Second, the absolute degrees of polymerization (DPs) of P4VPs were calculated based on ratio of peak areas, i.e., DP = $3/4[(A_i + A_j)/A_a]$, where A_a, A_i and A_j represent the peak area of peak (a), peak (i) and peak (j), respectively in Fig. S2.† Accordingly, the DP values were determined to be ∼21, ∼42, ∼74 and ∼198 for the prepared P4VPs. Thus, the four P4VPs are denoted as P4VP$_{21}$, P4VP$_{42}$, P4VP$_{74}$ and P4VP$_{198}$ according to their DPs.

Fig. 1a shows the SEC characterization result of P4VPs in DMF. The result demonstrates that all the RAFT polymerizations were conducted in a controlled manner, reflected in the small polydispersity indexes (M_w/M_n) ranging from ∼1.05 to ∼1.16. The number average molar mass (M_n) determined by SEC is ∼5.20 × 10^3 g mol^{-1}, ∼9.10 × 10^3 g mol^{-1}, ∼1.35 × 10^4 g mol^{-1} and ∼3.68 × 10^4 g mol^{-1} for P4VP$_{21}$, P4VP$_{42}$, P4VP$_{74}$ and P4VP$_{198}$, respectively, which are significantly larger than those determined by ^{1}H-NMR (Fig. S2†). The inconsistency is supposed to be attributed to the difference in hydrodynamic sizes of P4VP and polystyrene standard for a given molar mass. The chain length effect can be also observed from the UV-vis spectra shown in Fig. 2b, where the peak associated to trithiocarbonate (at ∼310 nm) gradually increases as M_n decreases, and the absorption peak located at ∼260 nm is assigned to absorption of pyridine rings.

Highly efficient ligand exchange reaction was utilized for the preparation of P4VP–Ru polymer–metal complexes. [Ru(bda)(pic)(DMSO)] (pic = 4-picoline) precursor was prepared according to the reported procedures (Fig. S3†).[23,24] The ligand exchange reaction was typically carried out at 45 °C for 12 h. The reaction solution was passed through a filter (450 nm) to remove the trace amount of insoluble substance before
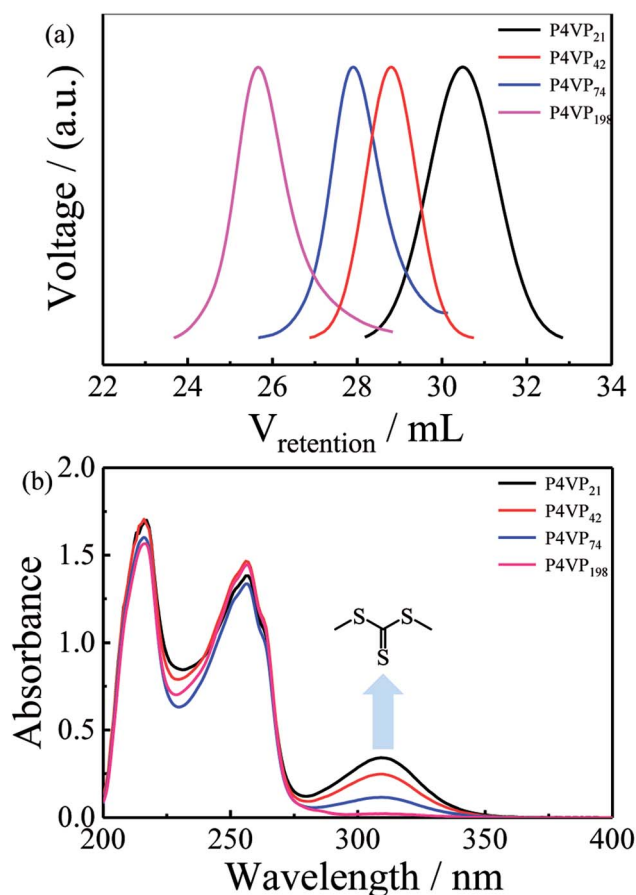

Fig. 1 (a) SEC curves of polymer ligands P4VPs with different chain lengths in DMF at T = 35 °C. (b) UV-vis spectra of polymer ligands P4VPs with different chain lengths in MeOH.

precipitation purification. Considering the limited solubility of P4VP–Ru complexes in MeOH and aqueous solution, the mass fraction (wt%) of Ru in P4VP–Ru complexes were controlled to be less than ∼5%. In the initial stage of exchange reaction, [Ru(bda)(pic)(DMSO)] precursor was insoluble in MeOH, while the reaction mixture became more and more clear as the reaction proceeded, indicating a much better solubility of P4VP–Ru complex because of the stronger solvation property of P4VP ligand. The successful preparation of P4VP–Ru complexes was first confirmed by FTIR measurement. As shown in Fig. 2b, P4VPs–Ru present the feature vibration bands of carboxylic ester (∼1650 cm^{-1}, blue band), signifying the successful installation of bda groups onto P4VP polymer backbone; moreover, the skeleton stretching vibration bands of pyridine rings (∼1600 cm^{-1}, red band) is clear for P4VPs–Ru. The ratio (I_1/I_2) of peak intensities of carboxylic ester (I_1, blue band) and pyridine (I_2, red band) in FTIR spectra can be used to semi-quantitatively estimate the exchange process (Fig. S4 and Table S1†). Namely, the I_1/I_2 ratios are typically 0.50–0.70 for P4VPs, but 0.90–0.95 for P4VPs–Ru. Fig. 2a further shows the comparative plots of UV-vis spectra of P4VPs and P4VPs–Ru at a fixed polymer concentration in MeOH. As shown, two newly emerging absorption bands located at 350–400 nm and 450–550 nm are obvious for P4VPs–Ru, which can be assigned to the
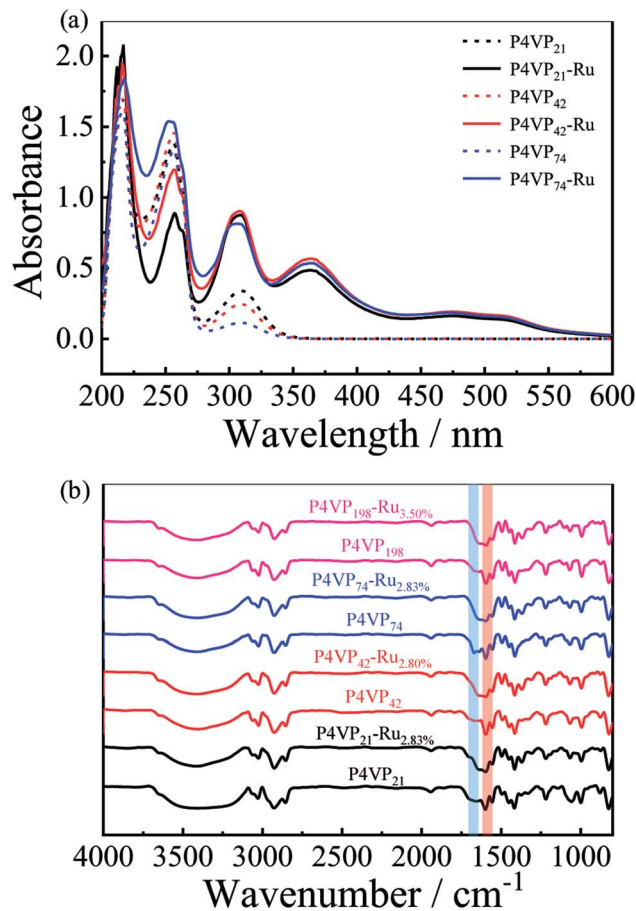
Fig. 2 (a) Comparative plots of UV-vis spectra of P4VPs and P4VPs–Ru with different chain lengths at a fixed concentration in MeOH, where the data for P4VP$_{198}$–Ru was not presented due to its poor solubility in MeOH. (b) FTIR spectra of P4VPs and P4VPs–Ru with different chain lengths, where the result of Ru ratio is from ICP-MS measurement.

Fig. 3 (a) Ratios of integral areas of ^{1}H-NMR signals of aromatic protons (A_{aro}) and aliphatic protons (A_{ali}) for P4VPs and P4VPs–Ru, where the result for P4VP$_{198}$–Ru is not obtained due to its poor solubility. (b) Theoretical and experimental mass fractions (wt%) of Ru element of P4VPs–Ru.

absorption feature of Ru^{II}. The intensities of the two bands seem to be similar for P4VPs–Ru with different chain lengths, indicating similar Ru loading amounts. Meanwhile, P4VP–Ru shows a good stability of Ru^{II} oxidation state in methanal (Fig. S5a†). It is worth noting that the initial attempt by using HNO$_3$ (aq, pH = 1.0) as a test solvent failed, as shown in Fig.-S5b,† probably due to the oxidation of Ru^{II} into Ru^{III} in acidic environment. After the addition of reducing agent ascorbic acid, the oxidized species Ru^{III} can be reversibly reduced to be Ru^{II} (Fig. S5b†).

Further, a combination of ^{1}H-NMR and inductively coupled plasma mass spectrometry (ICP-MS) was used to quantitatively analyze the loading amount of Ru in P4VPs–Ru. Compared with the bare P4VP, P4VP–Ru is supposed to own a higher mass fraction of aromatic protons due to the introduction of bda unit, which can be quantitatively reflected in the larger ratios (A_{aro}/A_{ali}) of integral areas of aromatic protons (A_{aro}) and aliphatic protons (A_{ali}) in ^{1}H-NMR spectra (Fig. S6†). Overall, the A_{aro}/A_{ali} ratio increases significantly after ligand exchange reaction (Fig. 3). The experimentally determined and theoretically calculated A_{aro}/A_{ali} ratios for P4VP and P4VPs–Ru are

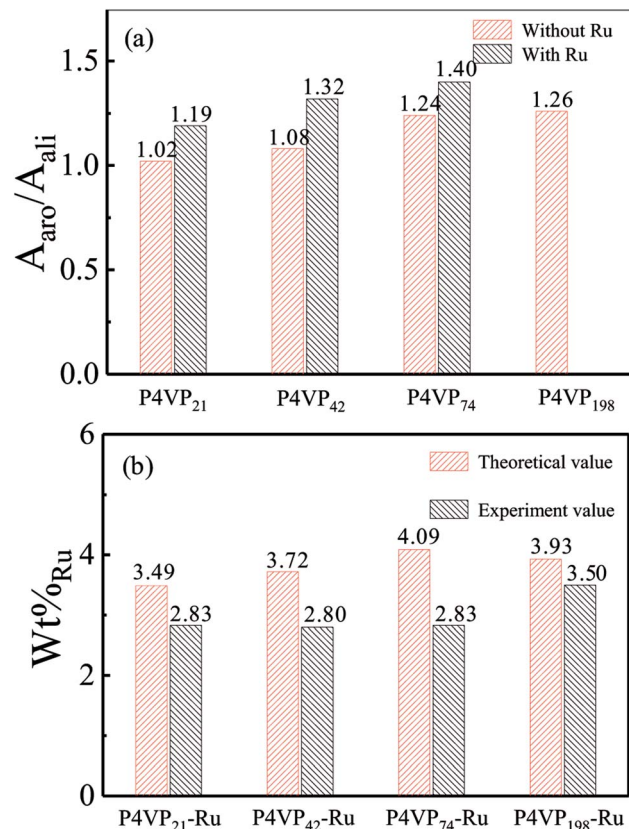summarized in Table S2.† Finally, ICP-MS measurement quantitatively determined the mass fractions (wt%) of Ru element of P4VPs–Ru (Fig. 3b and Table S3†). Overall, wt% varies from 2.8–3.5%, slightly smaller than the theoretical values (3.5–3.9%) calculated based on the feeding ratios, probably due to the incompletion of the ligand-exchange reaction. The redox potentials of P4VP$_{42}$–Ru and P4VP$_{198}$–Ru were determined by cyclic voltammetry (CV) in aqueous solution (pH = 1.0). The larger ΔE values is probably attributed to the slower electron transfer kinetics for polymer catalyst system. As shown in Fig. 4, when the scan was carried out from 0.2 to 1.2 V, the Ru$^{III/II}$ couple at ~0.70 V can be clearly observed as well as the electro-catalytic waves associated with the Ru$^{IV/III}$ (1.0 V). We noted that a small shift of ±0.02 V is observed for P4VP$_{42}$–Ru and P4VP$_{198}$–Ru, which is within the reasonable range. Moreover, the slight difference might also be related with the difference of degree of inter-chain coupling for different P4VP polymers. For comparison, the CV curve was also measured for reference complex [Ru(bda)(pic)$_2$]. Clearly, the result shows that the active Ru sites were successfully attached onto P4VP backbones.

By using these well characterized P4VP–Ru complexes as catalysts, we further explored how the polyelectrolyte ligand effect influences the catalytic behavior. From green chemistry
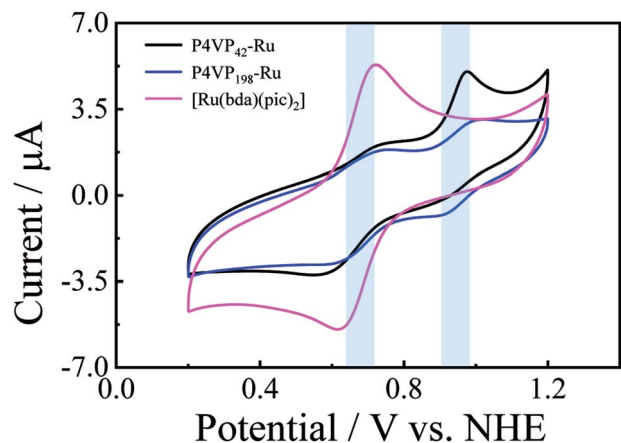
Fig. 4 Cyclic voltammograms (CVs) of P4VP$_{42}$–Ru and P4VP$_{198}$–Ru and small-molecule [Ru(bda)(pic)$_2$] in aqueous solution (pH = 1.0), where Pt wire was used as the counter electrode, and Ag/AgCl was used as the reference electrode (scan rate = 50 mV s^{-1}, $E_{NHE} = E_{Ag/AgCl}$ + 0.20).

perspective, the aqueous solution without organic co-solvent was used as the reaction medium. The catalytic water oxidation was performed by using cerium(IV) ammonium nitrate (CAN) as sacrificial oxidant. The reaction kinetics was monitored with an oxygen-sensor (Unisense), and the evolved amount of O$_2$ in gas space was analyzed by GC (Fig. S7†). In a typical experiment, 0.5 mL of P4VP–Ru solution (pH = 1.0) was degassed and then injected into O$_2$-free HNO$_3$ solution (9.5 mL,

pH = 1.0, [Ce^{IV}] = 0.105 M) in a sealed vial with rubber septum under constant stirring rate. Each P4VP–Ru solution was prepared by diluting a mother solution with polymer concentration of 1.0 mg mL^{-1}, and then pre-filtered through a 0.45 μm PTFE filter before injection.

Fig. 5a–d show the reaction time and catalyst concentration dependent oxygen evolution curves by using P4VP–Ru polyelectrolyte–metal complexes (PMCs) as catalysts. As expected, the oxygen evolution rate increases with the molar concentration of Ru (C_{Ru}), where C_{Ru} is the molar concentration of Ru in the final reaction solution with a total volume of 10 mL. Experimentally, the turnover frequency (TOF) was determined to be ~6.85 s^{-1} (P4VP$_{21}$–Ru, C_{Ru} = 14.00 μM), ~5.79 s^{-1} (P4VP$_{42}$–Ru, C_{Ru} = 13.86 μM), ~11.94 s^{-1} (P4VP$_{74}$–Ru, C_{Ru} = 14.00 μM) and ~3.01 s^{-1} (P4VP$_{198}$–Ru, C_{Ru} = 17.33 μM), respectively. According to Henry's law, the produced molecular oxygen in solution is supposed to successively undergo the nucleation, fusion and diffusion processes. Finally, the formed nano bubbles diffuse into gas phase to reach the gas–liquid phase equilibrium on thermodynamics. Thus, the interesting turning points from increase to decrease in Fig. 5 actually reflect the transition points where the O$_2$ diffusion rates start to exceed the O$_2$ evolution rates for P4VPs–Ru. In addition, the existence of turning points also indicates that the widely adopted pressure-sensor method by monitoring the internal pressure in gas phase might be not the best method for the real-time monitoring of the catalysis kinetics, due to the hysteresis of the oxygen diffusion process.
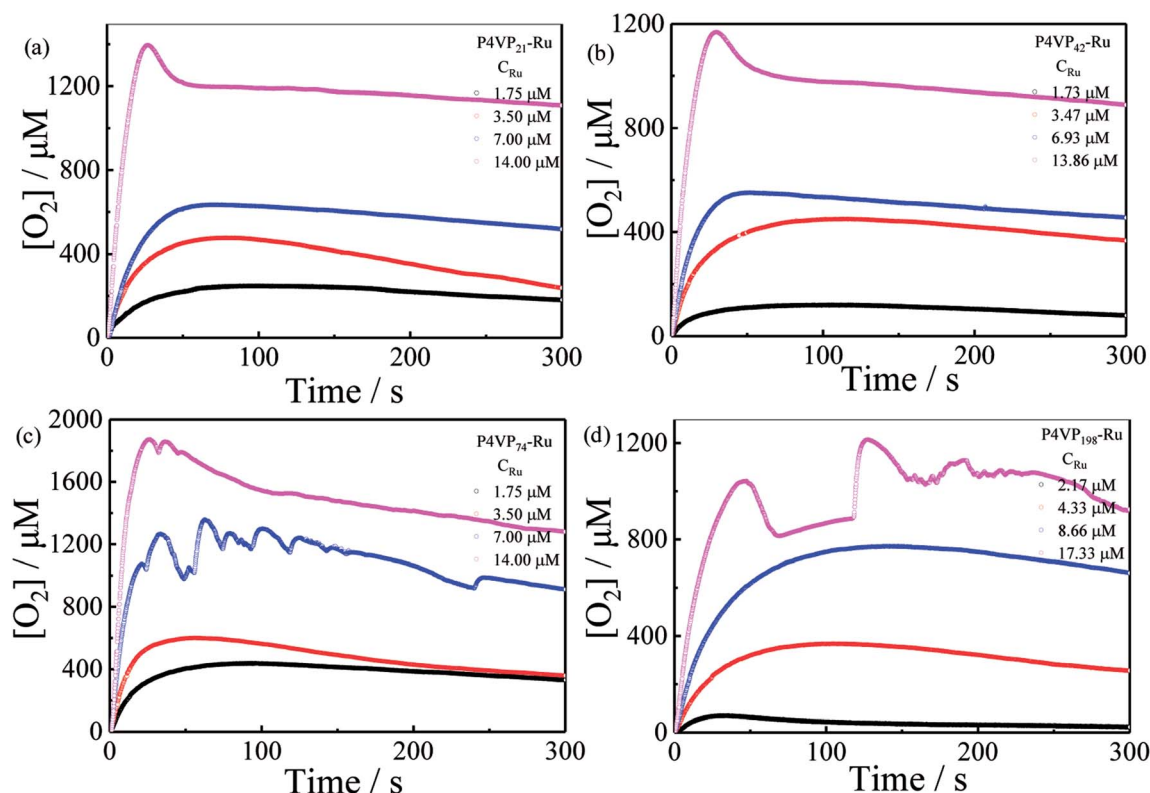

Fig. 5 (a)–(d) Reaction time (t) dependence of the oxygen concentration ([O$_2$]) in situ measured in solution by using P4VPs–Ru as catalysts, where [Ce^{IV}] = 100 mM and pH = 1.0.
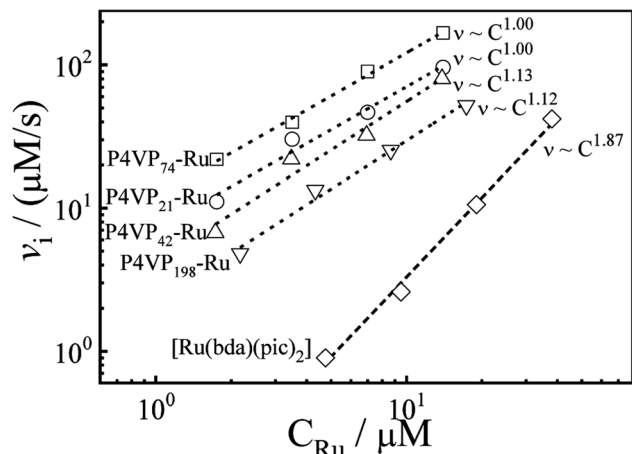
Fig. 6 Catalyst concentration (C_{Ru}) dependence of the initial oxygen evolution rate (v_i) for P4VPs–Ru and small-molecule [Ru(bda)(pic)$_2$], where [Ce^{IV}] = 100 mM and pH = 1.0.

Fig. 7 Number average molar mass (M_n) dependence of the turnover number (TON) of P4VP–Ru complexes, where [Ce^{IV}] = 100 mM, pH = 1.0 (HNO$_3$), and C_{Ru} = 14.00, 13.86, 14.00, 17.33 μM for P4VP$_{21}$–Ru, P4VP$_{42}$–Ru, P4VP$_{74}$–Ru and P4VP$_{198}$–Ru, respectively.

To obtain reliable kinetics data, the initial oxygen evolution rates (v_i) were calculated on the basis of data collected within the first few seconds (Fig. S8†), and the C_{Ru} values were calculated according to the ICP-MS results. As shown in Fig. 6, the quasi-linear relationships between v_i and C_{Ru} are established in log-scale, i.e., $v_i \sim C_{Ru}{}^{\alpha}$. The fitted value for scaling exponent α is ~1.00, ~1.13, ~1.00 and ~1.12 for P4VP$_{21}$, P4VP$_{42}$, P4VP$_{74}$ and P4VP$_{198}$, respectively. Surprisingly, the constant α shows no dependence on the chain length, which is different from our initial anticipation. However, these values are much smaller than those for homogeneous catalyst [Ru(bda)(pic)$_2$] ($\alpha \sim 2.0$) reported in literature.[18,25] Theoretically, the exponent α is related with the catalytic mechanism (vide infra).

In addition, the turnover numbers (TONs) for P4VP–Ru PMCs were measured by GC. As shown in Fig. 7, TON is ~1450 (P4VP$_{21}$–Ru, C_{Ru} = 14.00 μM), ~1620 (P4VP$_{42}$–Ru, C_{Ru} = 13.86 μM), ~1710 (P4VP$_{74}$–Ru, C_{Ru} = 14.00 μM) and ~1170 (P4VP$_{198}$–Ru, C_{Ru} = 17.33 μM), respectively, which are significantly larger than ~670 determined for [Ru(bda)(pic)$_2$] in our previous work.[25] The reason should be mainly attributed to the much stronger hydration ability of hydrophilic P4VP polymer ligand, which facilitates the diffusion and collision for water molecules around the catalytic centers of P4VPs–Ru. Numerically, P4VP$_{198}$–Ru shows the smallest TON, which is due to its much poorer solubility in HNO$_3$ aqueous solution. Overall, the above combined TOF and TON measurements clearly demonstrate that the polymer catalysts not only show high catalysis rates but also present excellent performances.

Generally, there are two widely accepted mechanisms for water oxidation at the metal centers, including: (1) single-site water nucleophilic attack (WNA) and (2) interaction between two metal oxide units (I2M).[17,26] It is well-known that the Ru(bda) based homogeneous catalysts generally oxidize water through bimolecular radical coupling process, i.e., I2M mechanism, which typically corresponds to the second-order kinetics, i.e., $v_i \sim C_{Ru}{}^{\alpha}$ ($\alpha = 2.0$).[18,25,27] In contrast, only a few studies reported the first-order kinetics for Ru(bda) based catalysis, which can be roughly divided into the following three
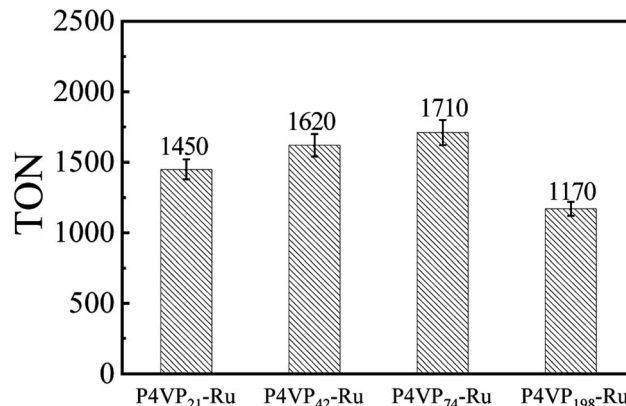
specific cases: (1) the ligand rigidity induced mechanism change;[18,19,27] (2) the restriction of motion of Ru catalytic centers located at interface of heterogeneous system;[28–30] (3) the intramolecular dimerization of two neighboring Ru^V=O species to form –O–O– bond.[31]

For example, Sun et al. reported that the replacement of bda with 1,10-phenanthroline-2,9-dicarboxylate (pda) could lead to the change of catalytic mechanism from I2M to WNA because of the flexibility difference of ligand structure.[27] Würthner et al. reported the preparation and catalysis behavior of Ru(bda) based supra-molecular macro-cycles as water oxidation catalysts, similarly, the supra-molecular catalysts were found to oxidize water via WNA mechanism because of the rigid ligand structure of supra-molecular assemblies.[18,31] Accordingly, the first-order reaction kinetics was observed in these studies. On the other hand, Ru(bda) based heterogeneous catalysts were also reported to catalyze water oxidation via WNA mechanism, which is generally explained by the restriction effect on motion of Ru catalytic centers located at interface of heterogeneous system. Namely, via kinetic isotope effect (KIE) study, Sun et al. found that the Ru(bda) supported electrodes could achieve electro-catalytic water oxidation via WNA mechanism.[29] Our recent work on heterogeneous Ru(bda) based polymer catalyst also revealed the key role of motion of catalytic centers in determining the catalytic mechanism in heterogeneous system.[25] In reality, the first-order kinetic could not only exist in mononuclear catalytic process, but also in bi-nuclear catalytic process in some cases. Namely, the recent work by Sun et al. has demonstrated that the Ru(bda) based tri-nuclear complex with flexible carbon–carbon single bond linkage, as homogeneous catalyst, could also present an apparent first-order kinetics, which was attributed to the occurrence of intramolecular radical coupling of two neighboring Ru centers, i.e. I2M pathway.[31]

The above discussion clearly clarifies that the determined reaction order is not a reliable criteria for the judgment of catalytic mechanism. Overall, for a given homogeneous catalysis system, if the first-order kinetics and the WNA mechanism are experimentally confirmed, the Ru(bda) based catalyst has to
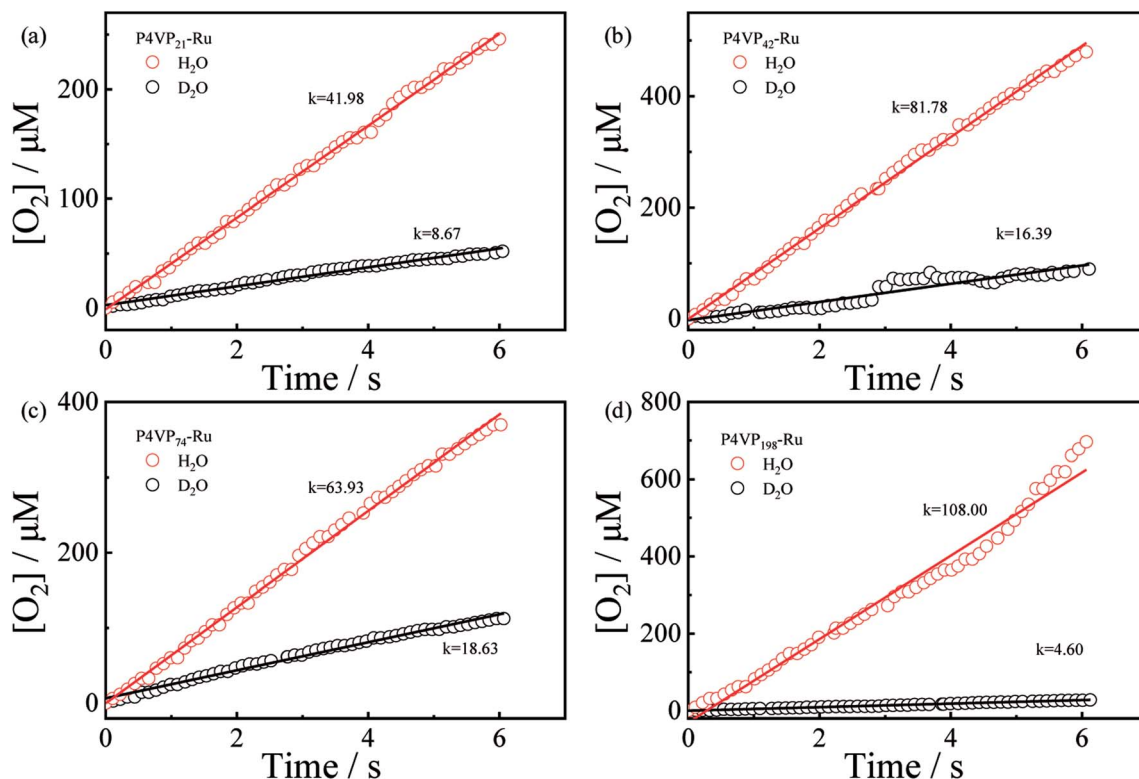
Fig. 8 (a)–(d) Reaction time (t) dependence of the oxygen concentration ([O_2]) in solution phase by using P4VP–Ru complexes as catalysts in H_2O and D_2O, respectively, where [Ce^{IV}] = 100 mM and pH = 1.0.

be composed of rigid ligands without torsional flexibility; in contrast, if the first-order kinetics and the I2M mechanism are experimentally confirmed, the Ru(bda) based catalyst has to consist of multiple Ru centers with flexible linkages between neighboring centers, favoring intramolecular radical coupling process.

The question left here is to confirm the catalytic mechanism for our observed first-order kinetics in P4VP–Ru PMC system, *i.e.*, whether catalysis is related with the WNA or I2M process. Intuitively, we supposed that our P4VP–Ru system should obey the I2M mechanism. This is because: (1) P4VP–Ru PMC catalyst is a typical type of multi-Ru catalyst; (2) the P4VP backbone is made of rotatable/flexible carbon–carbon single bonds. These two features make P4VP–Ru PMC system very similar with the tri-nuclear catalyst system reported by Sun *et al.*, where the backbone of tri-nuclear catalyst was also made of flexible carbon–carbon single bonds, and the catalytic mechanism was shown to be I2M mechanism.[19]

Thus, the kinetic isotope effect (KIE) study was further performed to provide clues to the catalytic mechanism. D_2O was used as reference solvent to explore whether O–H bond cleavage was involved in the rate-determining step. As shown in Fig. 8, for P4VP$_{21}$–Ru, P4VP$_{42}$–Ru and P4VP$_{74}$–Ru, the oxygen evolution rates in D_2O are significantly slower than those measured in H_2O. Quantitatively, the $KIE_{H/D}$ values are ∼4.84, ∼4.99 and ∼3.43, where the $KIE_{H/D}$ value is the ratio of the oxygen evolution rates in H_2O and D_2O. These values are much larger than the reported values for [Ru(bda)(pic)$_2$] ($KIE_{H/D}$ ∼ 0.9).[17–19] However, for high molar mass P4VP$_{198}$–Ru, its solubility in D_2O

was much poorer than that in H_2O due to the weaker hydration ability, and an apparent $KIE_{H/D}$ ∼ 23 was observed in the D_2O solution. Theoretically, the $KIE_{H/D}$ value is >2.0 if the proton-coupled process is involved (WNA); while it is normally between 0.7–1.5 if the catalytic mechanism is through I2M.[32] Clearly, the present result clarifies that both the inter-chain and intra-chain dimerization processes between Ru^V=O species are prohibited in P4VP–Ru system, though the flexible linkages are supposed to provide enough conformation entropy (entropy elasticity) for the occurrence of dimerization process. The mononuclear WNA is responsible for the observed first-order reaction kinetics.

The combined kinetics and KIE studies clearly indicate that, even if the neighboring Ru centers are chemically linked by flexible carbon–carbon single bonds, it is still possible to achieve water oxidation *via* the mononuclear WNA mechanism for a given multi-Ru catalyst system. From a perspective of polymer physics, we attributed the observed phenomenon to the unique slow diffusion and multi-charge properties of P4VP–Ru PMCs under catalysis condition, which are generally ignored in the study of small-molecule catalytic systems.

It is well-known that, for a given type of macromolecule in solution, the average diffusion coefficient ($\langle D \rangle$) generally decreases as the molecular size increases. For small molecules, no significant difference of diffusion coefficients is anticipated; however, it is not the case for polymer ligands due to their significant size effect. Thus, the diffusion behavior of P4VPs and P4VPs–Ru were comparatively investigated by dynamic light scattering (DLS) in MeOH. The obtained diffusion coefficient

distributions ($f(D)$) as well as hydrodynamic radius distributions ($f(R_h)$) are shown in Fig. S9 and S10.† Notably, three features could be extracted from the results in Fig. S9:† (i) the $\langle D \rangle$ values for P4VP–Ru complexes are nearly one order of magnitude smaller than those for P4VP precursors; (ii) P4VP–Ru complexes show much broader diffusion coefficient distributions compared with their P4VP precursors; (iii) $\langle D \rangle$ decreases as the chain length increases for both P4VP–Ru complexes and P4VP precursors. Accordingly, an opposite trend was observed for $f(R_h)$ (Fig. S10†).

Quantitatively, Fig. 9a shows the number average molar mass M_n dependence of the average diffusion coefficient $\langle D \rangle$ for these samples. The fitted results show that $\langle D \rangle$ is approximately scaled to M_n as $\langle D \rangle \sim M_n^{\alpha}$, where the exponent is close to 0.50 ± 0.05 for P4VPs and P4VPs–Ru, indicating the coil conformations for P4VPs and P4VPs–Ru chains in MeOH. More specifically, $\langle D \rangle$ for P4VPs–Ru are ~0.49 (P4VP$_{21}$–Ru), ~0.37 (P4VP$_{42}$–Ru), ~0.31 (P4VP$_{74}$–Ru) and ~0.36 (P4VP$_{198}$–Ru) times smaller than their corresponding precursors. It should be noted that only ~5% of the total pyridine units contain Ru centers, which is not supposed to significantly increase the molar masses of P4VP–Ru PMCs. Moreover, MeOH is a very good solvent for both P4VP backbone and Ru(bda) moiety, which precludes the possibility of inter-chain aggregation induced by solvophobic/solvophilic interaction. Reasonably, the significant decrease in $\langle D \rangle$ and increase in polydispersity could be attributed to the chain extension during the DMSO/pyridine ligand exchange reaction. In recent work by Meyer *et al.* on the interfacial deposition of Ru(bda) complexes,[33] they found that the pyridine/pyridine exchange could occur even at room temperature, though with a slow exchange rate. Thus, we expect that some of Ru(bda) centers might be simultaneously coordinated with pyridine units from two different P4VP precursor chains during exchange reaction (Fig. 9b). Overall, the determined $\langle D \rangle$ values for P4VP–Ru PMCs are 2–3 orders of magnitude smaller than those for small molecules (typically 4.0×10^{-10} to 9.0×10^{-10} m^2 s^{-1}). It is important to note that the slow diffusion of polymer catalyst can greatly enhance the suppression for the inter-chain collision and Ru dimerization processes, which

satisfactorily explains why the WNA mechanism was observed in this study. Note that the viscoelastic property of polymer ligand may also play a critical role in preventing the Ru dimerization process.

Reasonably, the slow diffusion feature of P4VPs–Ru can explain why the inter-chain collision is prohibited well, but it still does not help explain why the intra-chain dimerization is also prohibited. Note that the inter-Ru distance for Ru centers on the same P4VP backbone is very short, because the intra-chain Ru centers are separated averagely by only ~20 monomer units. For classic polyelectrolytes, the multi-charge electrostatic interaction is another key factor to be considered. It is well known that the pK_b of pyridine is ~8.8, which means that most of free pyridine units on polymer ligand should be in the protonated form during catalysis (pH = 1.0). The charged nature of P4VP–Ru PMCs was confirmed by zeta-potential measurement in aqueous solution at pH = 2.0. Fig. S11† shows that the measured zeta-potential is ~31.4, ~30.4, ~31.5 and ~29.2 for P4VP$_{21}$–Ru, P4VP$_{42}$–Ru, P4VP$_{74}$–Ru and P4VP$_{198}$–Ru, respectively; in contrast, the zeta-potential is ~0.0 ± 1.0 for [Ru(bda)(pic)$_2$], indicating a neutral state of small molecule catalyst. It should be noted that, for a suspending nanoparticle in solution, typically, it can be stabilized by the electrostatic repulsion interactions when the interfacial zeta-potential exceeds 15–20. Physically, it is not difficult to understand that the intra-chain electrostatic repulsion interaction can greatly suppress intra-chain Ru-dimerization process due to the enthalpy penalty, which satisfactorily explains why the I2M mechanism is not observed for P4VP–Ru PMC system. The result also reveals that though the existence of flexible linkages between Ru centers could provide enough conformation entropy for the occurrence of Ru-dimerization in small-molecule multi-nuclear system, the entropy elasticity could not overcome the electrostatic interaction energy in PMC system.

To further deepen our understanding of how the intra-chain electrostatic repulsion interaction affects the catalytic process, molecular dynamics simulations were carried out to quantitatively calculate the intra-chain collision probability
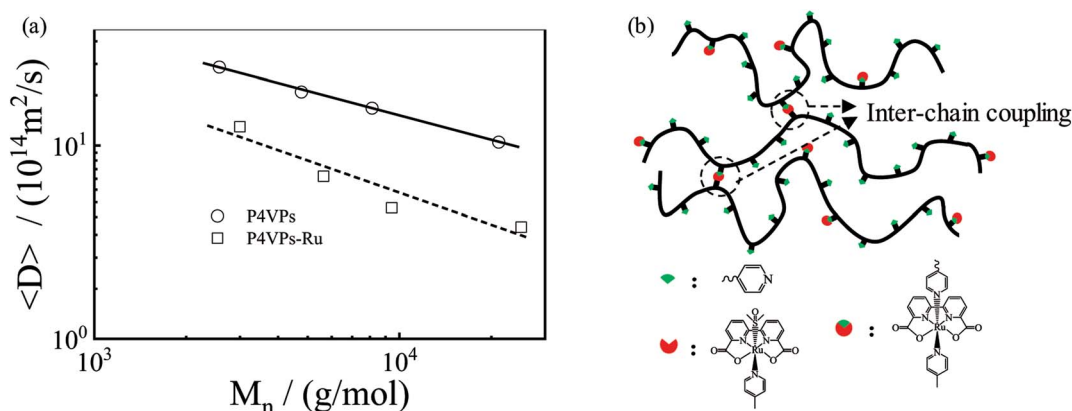

Fig. 9 (a) Number average molar mass (M_n) dependence of the average diffusion coefficient ($\langle D \rangle$) for P4VP–Ru complexes and their corresponding P4VP precursors in MeOH. (b) Schematic illustration of the possible inter-chain coupling reaction in the preparation of P4VP–Ru by ligand exchange reaction.
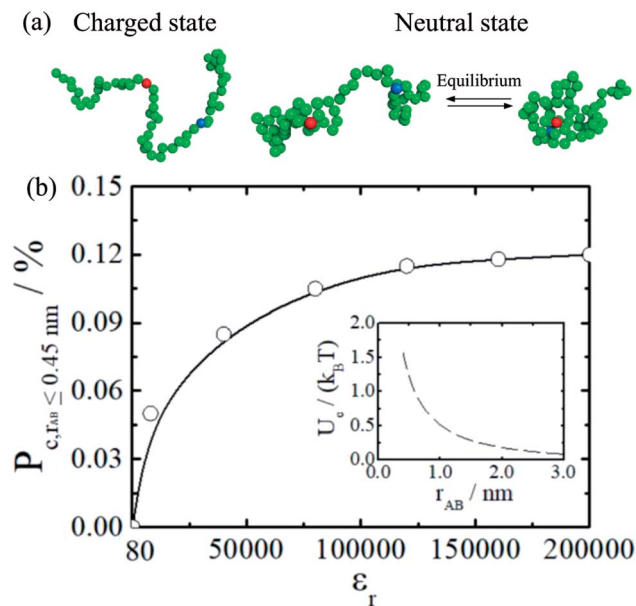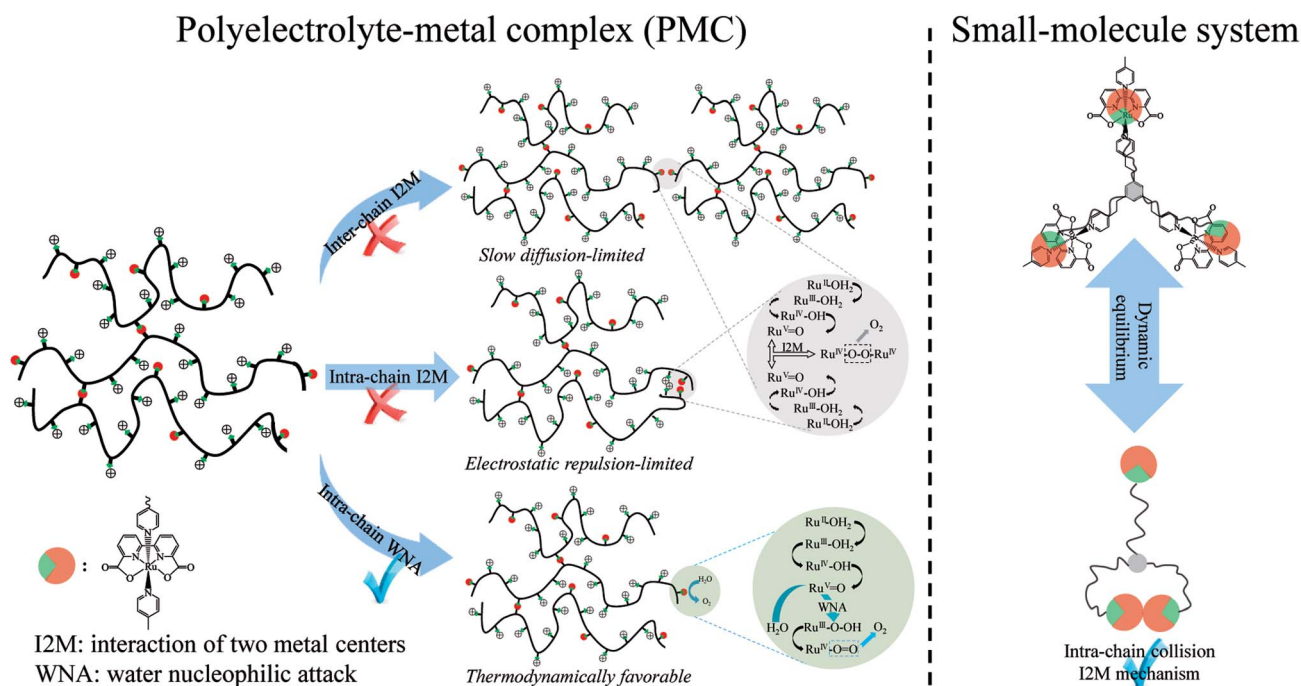
Fig. 10 (a) Schematic illustration of the chain conformations for charged and neutral polymer single chains, where the two catalytic centers (red and blue beads) are separated by 20 monomer units. (b) Dielectric constant dependence of the intra-chain collision probability (P_c) and the electrostatic potential (U_e) for two neighboring Ru centers.

(P_c) and the electrostatic potential (U_e) for two neighboring Ru centers (molecular dynamics simulation is only for P_c, U_e is calculated by Debye–Hückel Theory). Fig. 10a schematically illustrates the segment conformations for single polymer

chains in the charged and neutral states. The simulation result clearly shows that the electrostatic repulsive interaction causes the conformational extension of the single chain and strongly suppresses the collision of intra-chain Ru centers; while a dynamic equilibrium between the states of collision and separation can be established for a neutral polymer chain. Fig. 10b quantitatively shows how the collision probability P_c changes with the dielectric constant (ε_r) of the system. The result illustrates that when $\varepsilon_r = 80$ (without screening the electrostatic interaction), $P_c = 0$, which means that the collision for the two Ru units is completely inhibited in the charged state. As ε_r increases, the intra-chain electrostatic repulsion interaction decreases, and we observe that P_c exhibits an apparent non-linear increase. Eventually, P_c approaches to the limit of charge-neutral polymer. To highlight the energy barrier caused by the electrostatic repulsion, we further calculated the electrostatic potential (U_e) between two arbitrary segments i and j on polyelectrolyte backbone as a function of the separation distance r_{ij} at the ionic concentration of 0.1 M.

Clearly, U_e is approximately 1.5–2.0k_BT at $r_{ij} \sim 0.45$ nm, indicating that the thermal motion of PMC chains ($\sim k_BT$) could not overcome the electrostatic repulsive interaction to achieve a collision event, quantitatively explaining why the I2M mechanism is forbidden for PMC system, from a perspective of thermodynamics. Scheme 2 illustrates how the slow diffusion and multi-charge effects (electrostatic interaction) of polyelectrolyte ligand play a synergistically role in determining the catalytic mechanism and make the PMC system different from the small molecule tri-nuclear system.

Scheme 2 Schematic illustration of how the slow diffusion and multi-charge effects (electrostatic interaction) of polyelectrolyte ligand play a synergistically role in determining the catalytic mechanism and make the P4VP–Ru system different from the small molecule tri-nuclear system.[19]

Conclusions

In summary, we synthesized four poly(4-vinyl pyridine)–Ru(bda) (P4VP–Ru) polyelectrolyte–metal complexes (PMCs) with different chain lengths and controlled Ru loading amount. The chemical structures of P4VPs–Ru and their precursors P4VPs were confirmed by combining various characterization methods. The catalysis study reveals that these PMCs oxidize water *via* the single-site water nucleophilic attack (WNA) mechanism, rather than the interaction between two metal oxide units (I2M), which is unambiguously supported by the kinetics and kinetic isotope effect (KIE) measurements. In principle, due to the similar structural features between P4VP–Ru polymer system and tri-nuclear small-molecule system reported in literature (I2M, Sun *et al.*[31]), P4VP–Ru PMC system should also obey I2M mechanism, which is different from our experimental observation. Our study further reveals that the unique features of polyelectrolyte ligand (slow diffusion and multi-charge properties) are responsible for the observed mechanism difference between the two systems. The conclusion was strongly supported by dynamic light scattering characterization, zeta-potential measurement and molecular dynamics simulation. This study also highlights the fact that though the existence of flexible linkages between Ru centers could provide enough conformation entropy for the occurrence of Ru-dimerization in small-molecule multi-nuclear system, the entropy elasticity could not overcome the electrostatic interaction energy in PMC system. In addition to the mechanism difference, P4VPs–Ru catalysts also show excellent catalytic performance with high TONs (1200–1700), much higher than that of [Ru(bda)(pic)$_2$] reference. Overall, the present study has shown that the construction of PMCs is a novel polymer-based strategy to simultaneously regulate the catalytic mechanism and the catalytic performance of catalytic centers. We hope this work could not only be helpful for the understanding of the catalytic behavior of polymer-based catalysts in complex catalysis environments, but also provide practical guidance for the design of novel polymer-based catalyst systems.

Experimental section

Materials

Unless otherwise stated, all chemicals obtained from commercial suppliers were used without further purification. [Ru(bda)(pic)(DMSO)] (pic = 4-picoline) precursor was prepared according to the reported procedures,[29,34] and the characterization result is shown in Fig. S3.† The characterization result of RAFT agent is detailed in the ESI (Fig. S3†). 4-Vinyl pyridine (Sinopharm, 97%) was purified by distillation under reduced pressure over CaH$_2$. Dimethyl sulfoxide (DMSO, Sinopharm, AR) and dimethylformamide (DMF, Sinopharm, AR) were first dried with anhydrous magnesium sulfate and then distilled under reduced pressure prior to use. Methanol (MeOH, Sinopharm, AR) and pyridine (Sinopharm, AR) were distilled over CaH$_2$ just prior to use.

Characterization

Fourier transform infrared spectroscopy (FTIR) spectra were recorded on Nicolet™ iS™10 FTIR Spectrometer as KBr pellets. Ultraviolet and visible (UV-vis) absorption spectra were measured on a Shimadzu UV-3600 device. Nuclear magnetic resonance (NMR) spectra were recorded at 300 K on a Bruker Avance III Ascend 500 (500 MHz) spectrometer with a delay time (d1) set to 8 s by using deuterated chloroform (CDCl$_3$), deuterated methanol and deuterated water as the solvents, and tetramethylsilane (TMS) as the internal standard. The relative number- and weight-average molar masses (M_n and M_w) of P4VP samples were measured by size-exclusion chromatography (SEC) equipped with refractive index detector (RI) using DMF as eluent at a flow rate of 1.0 mL min^{-1}. A series of narrowly distributed polystyrene standards were use as calibration. Metal content was determined by inductively coupled plasma mass spectrometry (ICP-MS, X Series 2, Thermo fisher Scientific), where the sample was first digested by the concentrated nitric acid with a mass fraction of 70% at 70 °C for 24 h and further diluted by the dilute nitric acid with a mass fraction of 1% to achieve the appropriate concentration of Ru element. Zeta potential was measured by Zetasizer Nano ZS (Malvern) and 10 mg of the sample was dissolved in 1.0 mL a HNO$_3$ solution (pH = 2.0) before the measurement. Dynamic light scattering (DLS) was carried out on a commercial LLS spectrometer (ALV/DLS/SLS-5022F) equipped with a multi τ digital time correlator (ALV5000) and a cylindrical 22 mW UNIPHASE He–Ne laser (λ_0 = 632.8 nm) as the light source at fixed angle of 90°. The Laplace inversion of each measured intensity–intensity time correlation function $G^{(2)}(q,t)$ in the self-beating mode can lead to a line-width distribution $G(\Gamma)$, where q is the scattering vector. For dilute solutions, Γ is related to the translational diffusion coefficient D by $(\Gamma/q^2)_{q\to 0, C\to 0} \to D$, so that $G(\Gamma)$ can be converted into a transitional diffusion coefficient distribution $G(D)$ or further a hydrodynamic radius distribution $f(R_h)$ *via* the Stokes–Einstein equation, $R_h = (k_B T/6\pi\eta_0)/D$, where k_B, T and η_0 are the Boltzmann constant, the absolute temperature and the solvent viscosity, respectively. The time correlation functions were analyzed by both the cumulants and CONTIN analysis.

Synthesis of P4VP with different chain lengths by reversible addition-fragmentation chain transfer (RAFT) polymerization

The synthesis procedure for P4VP$_{21}$ is as follows: into a 5 mL dry glass tube with a magnetic stirring bar, RAFT agent (0.35 g, 0.95 mmol), 4-vinyl pyridine (2.00 g, 19.05 mmol), AIBN (15.60 mg, 95.20 μmol) and DMF (2.0 mL) were added successively. The polymerization tube was degassed by three freeze–vacuum–thaw cycles before sealed under vacuum. After 48 h of polymerization at 70 °C, the tube was cooled and the reaction mixture was concentrated before the resultant polymer was precipitated twice in an excess amount of cold ether. The final product was dried in vacuum for 12 h at 40 °C to give P4VP$_{21}$ (yield 88.09%, 2.07 g). The synthesis procedure for P4VP$_{42}$ is as follows: into a 5 mL dry glass tube with a magnetic stirring bar, RAFT agent (0.15 g, 0.42 mmol), 4-vinyl pyridine (2.00 g, 19.05 mmol), AIBN (6.94 mg, 42.30 μmol) and DMF (2.0 mL) were

added successively. The polymerization tube was degassed by three freeze–vacuum–thaw cycles before sealed under vacuum. After 48 h of polymerization at 70 °C, the tube was cooled and the reaction mixture was concentrated before the resultant polymer was precipitated twice in an excess amount of cold ether. The final product was dried in vacuum for 12 h at 40 °C to give P4VP$_{42}$ (yield 87.91%, 1.89 g). The synthesis procedure for P4VP$_{74}$ is as follows: into a 5 mL dry glass tube with a magnetic stirring bar, RAFT agent (0.09 g, 0.25 mmol), 4-vinyl pyridine (2.00 g, 19.05 mmol), AIBN (4.15 mg, 25.30 μmol) and DMF (2.0 mL) were added successively. The polymerization tube was degassed by three freeze–vacuum–thaw cycles before sealed under vacuum. After 48 h of polymerization at 70 °C, the tube was cooled and the reaction mixture was concentrated before the resultant polymer was precipitated twice in an excess amount of cold ether. The final product was dried in vacuum for 12 h at 40 °C to give P4VP$_{74}$ (yield 89.47%, 1.87 g). The synthesis procedure for P4VP$_{198}$ is as follows: into a 5 mL dry glass tube with a magnetic stirring bar, RAFT agent (35.67 mg, 95.25 μmol), 4-vinyl pyridine (2.00 g, 19.05 mmol), AIBN (3.57 mg, 9.53 μmol) and DMF (2.0 mL) were added successively. The polymerization tube was degassed by three freeze–vacuum–thaw cycles before sealed under vacuum. After 48 h of polymerization at 70 °C, the tube was cooled and the reaction mixture was concentrated before the resultant polymer was precipitated twice in an excess amount of cold ether. The final product was dried in vacuum for 12 h at 40 °C to give P4VP$_{198}$ (yield 92.04%, 1.85 g).

Synthesis of P4VP–Ru^{II}(bda) complex through ligand exchange reaction

The synthesis procedure for P4VP$_{21}$–Ru is as follows: into a 10 mL dry glass tube with a magnetic stirring bar, [Ru(bda)(pic)(DMSO)] (39.78 mg, 77.85 μmol), P4VP$_{21}$ (0.20 g, 77.85 μmol) and MeOH (5.0 mL) were added successively. The reaction tube was degassed by three freeze–vacuum–thaw cycles before sealed under vacuum. After 12 h of ligand exchange reaction at 45 °C, the tube was cooled and the reaction mixture was passed through a membrane filter (450 nm) to remove the trace amount of insoluble substance, and then concentrated before the resultant polymer was precipitated twice in an excess amount of cold ether. The final product was dried in vacuum for 12 h at 40 °C to give P4VP$_{21}$–Ru (yield 62.76%, 0.15 g). The synthesis procedure for P4VP$_{42}$–Ru is as follows: into a 10 mL dry glass tube with a magnetic stirring bar, [Ru(bda)(pic)(DMSO)] (42.82 mg, 83.79 μmol), P4VP$_{42}$ (0.20 g, 41.89 μmol) and MeOH (5.0 mL) were added successively. The reaction tube was degassed by three freeze–vacuum–thaw cycles before sealed under vacuum. After 12 h of ligand exchange reaction at 45 °C, the tube was cooled and the reaction mixture was passed through a membrane filter (450 nm) to remove the trace amount of insoluble substance, and then concentrated before the resultant polymer was precipitated twice in an excess amount of cold ether. The final product was dried in vacuum for 12 h at 40 °C to give P4VP$_{42}$–Ru (yield 65.84%, 0.16 g). The synthesis procedure for P4VP$_{74}$–Ru is as follows: into a 10 mL dry glass

tube with a magnetic stirring bar, [Ru(bda)(pic)(DMSO)] (50.26 mg, 98.35 μmol), P4VP$_{74}$ (0.20 g, 24.59 μmol) and MeOH (5.0 mL) were added successively. The reaction tube was degassed by three freeze–vacuum–thaw cycles before sealed under vacuum. After 12 h of ligand exchange reaction at 45 °C, the tube was cooled and the reaction mixture was passed through a membrane filter (450 nm) to remove the trace amount of insoluble substance, and then concentrated before the resultant polymer was precipitated twice in an excess amount of cold ether. The final product was dried in vacuum for 12 h at 40 °C to give P4VP$_{74}$–Ru (yield 71.93%, 0.18 g). The synthesis procedure for P4VP$_{198}$–Ru is as follows: into a 10 mL dry glass tube with a magnetic stirring bar, [Ru(bda)(pic)(DMSO)] (48.31 mg, 94.54 μmol), P4VP$_{198}$ (0.20 g, 9.45 μmol) and MeOH (5.0 mL) were added successively. The reaction tube was degassed by three freeze–vacuum–thaw cycles before sealed under vacuum. After 12 h of ligand exchange reaction at 45 °C, the tube was cooled and the reaction mixture was passed through a membrane filter (450 nm) to remove the trace amount of insoluble substance, and then concentrated before the resultant polymer was precipitated twice in an excess amount of cold ether. The final product was dried in vacuum for 12 h at 40 °C to give P4VP$_{198}$–Ru (yield 68.46%, 0.17 g).

Catalysis study on the chemically driven water oxidation reaction monitored by oxygen sensor and GC

The Ce^{IV} driven water oxidation reactions were performed under ambient conditions in a 25 mL glass vial with a rubber stopper. In each experiment, 548 mg of cerium(IV) ammonium nitrate (CAN) was dissolved in a 9.5 mL HNO$_3$ solution (pH = 1.0) in a 25 mL glass vial capped with a rubber stopper. The CAN solution was bubbling with N$_2$ for 10 min. Then, 0.5 mL of degassed P4VP–Ru solution (pH = 1.0) was injected into the reaction vial through a septum *via* an air-tight syringe under vigorous stirring. The produced O$_2$ in solution phase was recorded *in situ* by an oxygen sensor (Unisense, OX-N). Calibration of oxygen sensor was carried out before each measurement. For turnover number (TON) measurement, the reaction was stopped after 6 h, and 300 μL of the gas in head space were taken out with a gas-tight syringe and injected into the gas chromatograph (GC, Shimadzu, GC-2014ATF + SPL) with a thermal conductivity detector using argon as carrying gas. A few injections of known amount of O$_2$ were used as calibration standards. The O$_2$ concentration was obtained typically based on twice injections.

Study on the kinetic isotope effect (KIE) of P4VP–Ru^{II}(bda) catalysts in D$_2$O

The kinetic isotope effect experiments were carried out in H$_2$O and D$_2$O. In each experiment, 137 mg of CAN was dissolved in 2.375 mL of a HNO$_3$ solution (pH = 1.0, H$_2$O or D$_2$O) in a 5 mL glass vial capped with a rubber stopper. The CAN solution was bubbling with N$_2$ for 10 min. Then, 0.125 mL of degassed solution (1.0 mg mL^{-1}, pH = 1.0, H$_2$O or D$_2$O) of P4VP–Ru was injected into the reaction vial through a septum *via* an air-tight syringe under vigorous stirring. The produced O$_2$ in solution

phase was recorded *in situ* by an oxygen sensor (Unisense, OX-N). Calibration of oxygen sensor was carried out before each measurement.

Cyclic voltammetry

Electrochemical measurements were performed on a commercial instrument with a standard three-electrode configuration: reference electrode: Ag/AgCl (3 M KCl aqueous solution), working electrode: glassy carbon electrode, auxiliary electrode: Pt slice (~2.5 cm^2). 6 mg of P4VP–Ru complex was dissolved in 2 mL of a HNO$_3$ solution (pH = 1.0) as electrolyte solution, and 1 mg of [Ru(bda)(pic)$_2$] was also dissolved in 2 mL of a HNO$_3$ solution (pH = 1.0) as a contrast. All solutions were bubbling with N$_2$ in the preparation process and keep N$_2$ environment during the measurement. Scan rate was fixed at 50 mV s^{-1}. The potentials measured against the Ag/AgCl (3 M KCl aqueous solution) reference electrode were transferred into potentials against the Normal Hydrogen Electrode (NHE) by addition of +0.209 V to the obtained values.

Molecular dynamics simulation

In our model, a single charged polymer and the counter-ions are immersed in the solvent molecules. We coarse-grain all polymer segments, solvent molecules and counter-ions as spherical particles, and employ the Weeks–Chandler–Andersen (WCA) potential to account for the excluded volume interactions between the particles:

$$U_{ij}^{WCA}(r_{ij}) = \begin{cases} 4\varepsilon_{LJ}\left[\left(\frac{\sigma}{r_{ij}}\right)^{12} - \left(\frac{\sigma}{r_{ij}}\right)^{6}\right] + \varepsilon_{LJ} & , r_{ij} \le r_c \\ 0 & , r_{ij} > r_c \end{cases} \quad (1)$$

where ε_{LJ} is the depth of the potential well, σ denotes the effective diameter of the particles, and r_{ij} is the separation distance between particles i and j, The cutoff radius is set to be $r_c = 2^{1/6}\sigma$. For simplicity, all polymer segments, counter-ions, and solvent particles are assigned the same mass m, size σ (which corresponds to 0.4 nm in real units), and ε_{LJ} parameter. The continuous segments of the polymer are connected with the finite extensible nonlinear elastic (FENE) potential:

$$U_{FENE}(r_b) = -\frac{1}{2}kR_0^2 \ln\left[1 - \left(\frac{r_b}{R_0}\right)^2\right] \quad (2)$$

where r_b denotes the distance between connected segments. We set the parameters $k = 30\varepsilon_{LJ}/\sigma^2$ and $R_0 = 1.5\sigma$ to avoid the bond crossing. Each segment of the polymer takes a monovalent positive charge at its center and all charged particles (polymer segments and the counter-ions) interact *via* Coulomb potential through the particle-particle particle-mesh method.[35]

We set the size of simulation box to be $L = 16\sigma$. The polymer is composed of $N_p = 62$ segments, with the 21th and the 42nd ones characterized as segments containing Ru centers, respectively. The system is composed of a total of 3276 particles, and therefore, the concentration of the charged segments in the real units is consistent with our experiments. We vary the dielectric constant of the system from $\varepsilon_r = 80$ (which corresponds to

water) to $\varepsilon_r = 200\,000$. The velocity-Verlet algorithm is used to integrate the equation of motion, and the simulations are performed in the NVT ensemble with periodic conditions in three dimensions. We set the temperature to be 1.0, which corresponds to 300 K in the real units, and the time step in solving the equation of motion is $t = 0.005$. All the simulations are performed using Large-scale Atomic/Molecular Massively Parallel Simulator (LAMMPS) developed by Sandia National Laboratories.[36] The final data are taken from 10^3 to 10^4 statistically independent samples, each after an equilibration time of the order of 10^6 MD steps.

Conflicts of interest

There are no conflicts to declare.

Notes and references

1 G. Pasut and F. M. Veronese, Polymer–drug conjugation, recent achievements and general strategies, *Prog. Polym. Sci.*, 2007, **32**, 933–961.
2 A. San Juan, D. Letourneur and V. A. Izumrudov, Quaternized Poly(4-Vinylpyridine)s as Model Gene Delivery Polycations: Structure–Function Study by Modification of Side Chain Hydrophobicity and Degree of Alkylation, *Bioconjugate Chem.*, 2007, **18**, 922–928.
3 A. C. Jandrey, A. P. de Aguiar, M. R. M. P. de Aguiar, L. C. de Santa Maria, J. L. Mazzei and I. Felzenszwalb, Iodine–poly(2-vinylpyridine-co-styrene-co-divinylbenzene) charge transfer complexes with antibacterial activity, *Eur. Polym. J.*, 2007, **43**, 4712–4718.
4 M. S. Chernov'yants, I. V. Burykin, R. V. Pisanov and O. A. Shalu, Synthesis and antimicrobial activity of poly(N-methyl-4-vinylpyridinium triiodide), *Pharm. Chem. J.*, 2010, **44**, 61–63.
5 L. Larabi, Y. Harek, M. Traisnel and A. Mansri, Synergistic Influence of Poly(4-Vinylpyridine) and Potassium Iodide on Inhibition of Corrosion of Mild Steel in 1M HCl, *J. Appl. Electrochem.*, 2004, **34**, 833–839.
6 O. Krim, A. Elidrissi, B. Hammouti, A. Ouslim and M. S. Benkaddour, Synthesis, Characterization, and Comparative Study of Pyridine Derivatives as Corrosion Inhibitors of Mild Steel in HCl Medium, *Chem. Eng. Commun.*, 2009, **196**, 1536–1546.
7 G. Boschloo, L. Häggman and A. Hagfeldt, Quantification of the Effect of 4-tert-Butylpyridine Addition to I-/I3- Redox Electrolytes in Dye-Sensitized Nanostructured TiO$_2$ Solar Cells, *J. Phys. Chem. B*, 2006, **110**, 13144–13150.

8 H. Wang, X. Liu, Z. Wang, H. Li, D. Li, Q. Meng and L. Chen, Effect of Iodine Addition on Solid-State Electrolyte LiI/3-Hydroxypropionitrile (1:4) for Dye-Sensitized Solar Cells, *J. Phys. Chem. B*, 2006, **110**, 5970–5974.

9 N. Leadbeater and M. Marco, Preparation of Polymer-Supported Ligands and Metal Complexes for Use in Catalysis, *Chem. Rev.*, 2002, **102**, 3217–3274.

10 X. Xi, Y. Liu, J. Shi and S. Cao, Palladium complex of poly(4-vinylpyridine-co-acrylic acid) for homogeneous hydrogenation of aromatic nitro compounds, *J. Mol. Catal. A: Chem.*, 2003, **192**, 1–7.

11 D. Wang, W. Liu, F. Bian and W. Yu, Magnetic polymer nanocomposite-supported Pd: an efficient and reusable catalyst for the Heck and Suzuki reactions in water, *New J. Chem.*, 2015, **39**, 2052–2059.

12 R. Saladino, V. Neri, E. Mincione and P. Filippone, Selective oxidation of phenol and anisole derivatives to quinones with hydrogen peroxide and polymer-supported methylrhenium trioxide systems, *Tetrahedron*, 2002, **58**, 8493–8500.

13 H. S. Kim, J. J. Kim, H. N. Kwon, M. J. Chung, B. G. Lee and H. G. Jang, Well-Defined Highly Active Heterogeneous Catalyst System for the Coupling Reactions of Carbon Dioxide and Epoxides, *J. Catal.*, 2002, **205**, 226–229.

14 B. Gao, D. Kong and Y. Zhang, Preparation and catalytic activity of P4VP–Cu(II) complex supported on silica gel, *J. Mol. Catal. A: Chem.*, 2008, **286**, 143–148.

15 S. Xu, J. He and S. Cao, Catalytic behaviors of the palladium complex of MgO-supported melamino-formaldehyde polymer for hydrogenations of different substrates, *J. Mol. Catal. A: Chem.*, 1999, **147**, 155–158.

16 A. V. Dobrynin and M. Rubinstein, Theory of polyelectrolytes in solutions and at surfaces, *Prog. Polym. Sci.*, 2005, **30**, 1049–1118.

17 L. Duan, F. Bozoglian, S. Mandal, B. Stewart, T. Privalov, A. Llobet and L. Sun, A molecular ruthenium catalyst with water-oxidation activity comparable to that of photosystem II, *Nat. Chem.*, 2012, **4**, 418–423.

18 M. Schulze, V. Kunz, P. D. Frischmann and F. Würthner, A supramolecular ruthenium macrocycle with high catalytic activity for water oxidation that mechanistically mimics photosystem II, *Nat. Chem.*, 2016, **8**, 576–583.

19 V. Kunz, M. Schulze, D. Schmidt and F. Würthner, Trinuclear Ruthenium Macrocycles: Toward Supramolecular Water Oxidation Catalysis in Pure Water, *ACS Energy Lett.*, 2017, **2**, 288–293.

20 L. Li and Z. Cai, Structure control and photocatalytic performance of porous conjugated polymers based on perylene diimide, *Polym. Chem.*, 2016, **7**, 4937–4943.

21 L. Li, Z. Cai, Q. Wu, W.-Y. Lo, N. Zhang, L. X. Chen and L. Yu, Rational Design of Porous Conjugated Polymers and Roles of Residual Palladium for Photocatalytic Hydrogen Production, *J. Am. Chem. Soc.*, 2016, **138**, 7681–7686.

22 L. Li, W.-y. Lo, Z. Cai, N. Zhang and L. Yu, Donor–Acceptor Porous Conjugated Polymers for Photocatalytic Hydrogen Production: The Importance of Acceptor Comonomer, *Macromolecules*, 2016, **49**, 6903–6909.

23 L. Duan, L. Wang, A. K. Inge, A. Fischer, X. Zou and L. Sun, Insights into Ru-Based Molecular Water Oxidation Catalysts: Electronic and Noncovalent-Interaction Effects on Their Catalytic Activities, *Inorg. Chem.*, 2013, **52**, 7844–7852.

24 F. Li, B. Zhang, X. Li, Y. Jiang, L. Chen, Y. Li and L. Sun, Highly Efficient Oxidation of Water by a Molecular Catalyst Immobilized on Carbon Nanotubes, *Angew. Chem., Int. Ed.*, 2011, **50**, 12276–12279.

25 T. Zheng and L. Li, {[Ru(bda)]$_x$L$_y$}$_n$ cross-linked coordination polymers: toward efficient heterogeneous catalysis for water oxidation in an organic solvent-free system, *New J. Chem.*, 2018, **42**, 2526–2536.

26 J. J. Concepcion, J. W. Jurss, J. L. Templeton and T. J. Meyer, One Site is Enough. Catalytic Water Oxidation by [Ru(tpy)(bpm)(OH$_2$)]$^{2+}$ and [Ru(tpy)(bpz)(OH$_2$)]$^{2+}$, *J. Am. Chem. Soc.*, 2008, **130**, 16462–16463.

27 L. Tong, L. Duan, Y. Xu, T. Privalov and L. Sun, Structural Modifications of Mononuclear Ruthenium Complexes: A Combined Experimental and Theoretical Study on the Kinetics of Ruthenium-Catalyzed Water Oxidation, *Angew. Chem., Int. Ed.*, 2011, **50**, 445–449.

28 R. Staehle, L. Tong, L. Wang, L. Duan, A. Fischer, M. S. G. Ahlquist, L. Sun and S. Rau, Water Oxidation Catalyzed by Mononuclear Ruthenium Complexes with a 2,2′-Bipyridine-6,6′-dicarboxylate (bda) Ligand: How Ligand Environment Influences the Catalytic Behavior, *Inorg. Chem.*, 2014, **53**, 1307–1319.

29 F. Li, K. Fan, L. Wang, Q. Daniel, L. Duan and L. Sun, Immobilizing Ru(bda) Catalyst on a Photoanode *via* Electrochemical Polymerization for Light-Driven Water Splitting, *ACS Catal.*, 2015, **5**, 3786–3790.

30 R. Matheu, L. Francàs, P. Chernev, M. Z. Ertem, V. Batista, M. Haumann, X. Sala and A. Llobet, Behavior of the Ru-bda Water Oxidation Catalyst Covalently Anchored on Glassy Carbon Electrodes, *ACS Catal.*, 2015, **5**, 3422–3429.

31 L. L. Zhang, Y. Gao, Z. Liu, X. Ding, Z. Yu and L. C. Sun, A trinuclear ruthenium complex as a highly efficient molecular catalyst for water oxidation, *Dalton Trans.*, 2016, **45**, 3814–3819.

32 H. Yamada, W. F. Siems, T. Koike and J. K. Hurst, Mechanisms of Water Oxidation Catalyzed by the cis,cis-[(bpy)$_2$Ru(OH$_2$)]$_2$O^{4+} Ion, *J. Am. Chem. Soc.*, 2004, **126**, 9786–9795.

33 D. Wang, S. L. Marquard, L. Troian-Gautier, M. V. Sheridan, B. D. Sherman, Y. Wang, M. S. Eberhart, B. H. Farnum, C. J. Dares and T. J. Meyer, Interfacial Deposition of Ru(II) Bipyridine-Dicarboxylate Complexes by Ligand Substitution for Applications in Water Oxidation Catalysis, *J. Am. Chem. Soc.*, 2018, **140**, 719–726.

34 L. Wang, M. Mirmohades, A. Brown, L. Duan, F. Li, Q. Daniel, R. Lomoth, L. Sun and L. Hammarström, Sensitizer-Catalyst Assemblies for Water Oxidation, *Inorg. Chem.*, 2015, **54**, 2742–2751.

35 R. W. Hockney and J. W. Eastwood, *Computer simulation using particles*, Taylor & Francis Group, New York, 1988.

36 S. Plimpton, Fast Parallel Algorithms for Short-Range Molecular Dynamics, *J. Comput. Phys.*, 1995, **117**, 1–19.